LAWRENCE
LIVERMORE
NATIONAL
LABORATORY

LLNL-JRNL-768104-DRAFT

Molybdenum Isotopes in Presolar Silicon Carbide Grains Reveal Details of s-Process Nucleosynthesis in Parent Stars

T. Stephan, R. Trappitsch, P. Boehnke, P. Hoppe, A. M. Davis, M. J. Pellin, O. S. Pardo

February 20, 2019

The Astrophysical Journal

Disclaimer

This document was prepared as an account of work sponsored by an agency of the United States government. Neither the United States government nor Lawrence Livermore National Security, LLC, nor any of their employees makes any warranty, expressed or implied, or assumes any legal liability or responsibility for the accuracy, completeness, or usefulness of any information, apparatus, product, or process disclosed, or represents that its use would not infringe privately owned rights. Reference herein to any specific commercial product, process, or service by trade name, trademark, manufacturer, or otherwise does not necessarily constitute or imply its endorsement, recommendation, or favoring by the United States government or Lawrence Livermore National Security, LLC. The views and opinions of authors expressed herein do not necessarily state or reflect those of the United States government or Lawrence Livermore National Security, LLC, and shall not be used for advertising or product endorsement purposes.

Accepted for publication in *The Astrophysical Journal*

Molybdenum Isotopes in Presolar Silicon Carbide Grains: Details of *s*-Process Nucleosynthesis in Parent Stars and Implications for *r*- and *p*-Processes

Thomas Stephan[1,2], Reto Trappitsch[1,2,*], Peter Hoppe[3], Andrew M. Davis[1,2,4], Michael J. Pellin[1,2,4,5], and Olivia S. Pardo[1,2]

[1] Department of the Geophysical Sciences, The University of Chicago, 5734 S Ellis Ave, Chicago, IL 60637, USA

[2] Chicago Center for Cosmochemistry, Chicago, IL, USA

[3] Max Planck Institute for Chemistry, 55128 Mainz, Germany

[4] The Enrico Fermi Institute, The University of Chicago, Chicago, IL 60637, USA

[5] Materials Science Division, Argonne National Laboratory, Argonne, IL 60439, USA

Corresponding author: Thomas Stephan

tstephan@uchicago.edu

[*] Present address: Nuclear and Chemical Sciences Division, Lawrence Livermore National Laboratory, Livermore, CA 94550, USA.

Abstract

We have analyzed molybdenum isotopes, together with strontium and barium isotopes, in 18 presolar silicon carbide grains using CHILI, the Chicago Instrument for Laser Ionization, a resonance ionization mass spectrometer. All observed isotope ratios can be explained by mixtures of pure *s*-process matter with isotopically solar material. Grain residues were subsequently analyzed for carbon, nitrogen, silicon, and sulfur isotopes, and a subset also for ^{26}Al-^{26}Mg systematics using the NanoSIMS. These analyses showed that all but one grain are mainstream grains, most probably coming from low-mass asymptotic giant branch (AGB) stars. One grain is of the AB type, for which the origin is still a matter of debate. The high precision of molybdenum isotope measurements with CHILI provides the best estimate to date for *s*-process molybdenum made in low-mass AGB stars. The average molybdenum isotopic abundances produced by the *s*-process found in the analyzed mainstream SiC grains are 0 % ^{92}Mo, 0.73 % ^{94}Mo, 13.30 % ^{95}Mo, 36.34 % ^{96}Mo, 9.78 % ^{97}Mo, 39.42 % ^{98}Mo, and 0.43 % ^{100}Mo. Solar molybdenum can be explained as a combination of 45.9 % *s*-process, 30.6 % *r*-process, and 23.5 % *p*-process contributions. Furthermore, the observed variability in the individual grain data provides insights into the variability of conditions (neutron density, temperature, and timescale) during *s*-process nucleosynthesis in the grains' parent stars as they have subtle effects on specific molybdenum isotope ratios. Finally, the results suggest that the ratio between *p*- and *r*-process molybdenum in presolar SiC from many different types of parent stars is $Mo_p/Mo_r = 0.767$, the

value inferred for the Solar System and consistent with what has been found in bulk samples and leachates of primitive meteorites.

Key words: circumstellar matter — dust, extinction — meteorites, meteors, meteoroid — nuclear reactions, nucleosynthesis, abundances — stars: AGB and post-AGB

1. Introduction

Presolar silicon carbide (SiC) grains found, e.g., in primitive meteorites exhibit large isotopic anomalies in major and minor elements, which can be used to link them to their stellar origins. Such grains condensed in the winds of evolved stars and in the ejecta of stellar explosions. They represent samples of stardust that can be analyzed in the laboratory. Based on their carbon, silicon, and nitrogen isotopic compositions, presolar SiC grains are divided into distinct populations. About 95 % of the grains, classified as mainstream (~90 %), Y (a few %), and Z (a few %) grains, are attributed to low-mass (1.5–3 $M_{\odot}$) asymptotic giant branch (AGB) stars with approximately solar (mainstream grains) and perhaps subsolar (Y and Z grains) metallicities. Other types include C (~0.1 %) and X grains (~1%), which are believed to come from Type II supernovae, putative nova grains (~0.1 %), and AB grains (~4–5 %), for which their origins are still a matter of debate (J-type carbon stars, born-again AGB stars, and/or Type II supernovae). More comprehensive overviews of presolar grains are given in the literature (e.g., Davis 2011; Zinner 2014; Nittler & Ciesla 2016).

Major fractions of strontium, molybdenum, and barium in the Solar System are synthesized by the *s*-process in AGB stars. Furthermore, these elements are particularly sensitive to branching along the *s*-process path between neutron capture and β-decay and can therefore be used to determine physical conditions including neutron density, temperature, and timescale during nucleosynthesis. Previous analyses of mainstream SiC grains confirmed their connection to the *s*-process for these elements (Ott & Begemann 1990a, b; Zinner et al. 1991; Prombo et al. 1993; Nicolussi et al. 1998a, b; Savina et al. 2003a; Lugaro et al. 2003; Podosek et al. 2004; Yin et al. 2006; Barzyk et al. 2007; Marhas et al. 2007; Ávila et al. 2013; Liu et al. 2014b, 2015, 2017b; Stephan et al. 2018).

We present new strontium, molybdenum, and barium isotopic data for SiC grains, obtained by resonance ionization mass spectrometry (RIMS) with the Chicago Instrument for Laser Ionization (CHILI; Stephan et al. 2016) at the University of Chicago. In addition, carbon, nitrogen, silicon, and sulfur isotopic data, together with ^{26}Al-^{26}Mg systematics on a subset of grains, were measured with secondary ion mass spectrometry (SIMS) using the CAMECA NanoSIMS 50 at the Max Planck Institute for Chemistry in Mainz, Germany (Hoppe et al. 2013). Here, we focus especially on molybdenum isotopic compositions.

Molybdenum is a favorable element for studying nucleosynthesis, because of the variety of sources represented in solar[1] composition and in presolar grains. The fact that solar abundances

[1] The precise isotopic compositions of carbon, silicon, strontium, molybdenum, and barium in the Sun are not known; we use "solar" as a shorthand, under the assumption that terrestrial and solar compositions of these elements are the same, at least at the permil level. Solar and terrestrial ^{14}N/^{15}N are significantly different from one another, and here, we refer to the measured solar composition (Marty et al. 2011).

of all molybdenum isotopes are the same within a factor of less than three makes isotopic measurements easier. Molybdenum has seven stable isotopes (see Figure 1): *p*-process ^{92}Mo and ^{94}Mo; mixed *s*- and *r*-process ^{95}Mo, ^{97}Mo, and ^{98}Mo; *s*-process-only ^{96}Mo; and *r*-process ^{100}Mo. The *p*-process molybdenum isotopes are bypassed by the main *s*-process path, as is *r*-process ^{100}Mo (Figure 1). However, some ^{94}Mo and ^{100}Mo could be synthesized in minor *s*-process reactions as shown in Figure 1. The origin of the *p*-process isotopes is not well understood, they could be produced by proton capture and/or photodisintegration. Molybdenum-92 and ^{94}Mo are of exceptionally high abundance compared to the *p*-process isotopes of most heavy elements.

CHILI enables us to measure these isotopes in presolar grains with unprecedented precision, allowing conclusions to be drawn about the variability of conditions in stellar environments during nucleosynthesis.

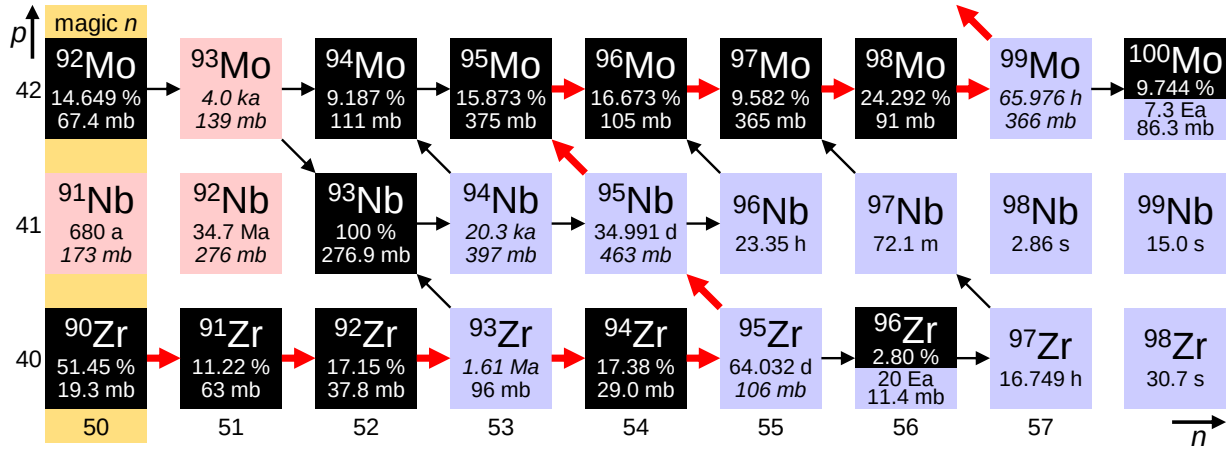

Figure 1. A section of the chart of the nuclides showing the main *s*-process path (thick, red arrows) as well as minor *s*-process reactions (thin, black arrows). For each stable isotope (black squares), the terrestrial "representative isotopic abundance" is given according to Meija et al. (2016), which for these elements are expected to be identical with overall Solar System abundances, at least within the uncertainties discussed here. The half-lives at room temperature are given for unstable nuclides (Audi et al. 2012), with numbers in italics indicating strong temperature dependence, more than a factor of two variation in half-life at temperatures between 5×10^7 and 5×10^8 K according to Takahashi & Yokoi (1987). Neutron capture cross sections are given as Maxwellian-averaged cross sections (MACS) at kT = 30 keV from the Karlsruhe Astrophysical Database of Nucleosynthesis in Stars (KADoNiS v1.0; Dillmann et al. 2014) for each nuclide; numbers in italics are based on theoretical calculations only. The uncertainties of MACS that are based on theoretical calculations alone were estimated in KADoNiS v1.0 to be 25 % or even, in the case of ^{93}Mo, 50 %. For other MACS, uncertainties between 1.8 % and 15 % were given in KADoNiS v1.0. Zirconium-96 and ^{100}Mo can decay by double beta decay, but not on an astrophysically relevant timescale.

2. Samples and analytical methods

2.1. Samples

Presolar SiC grains extracted from the Murchison CM2 meteorite were analyzed in this study. Grains are from the 1.5–3 µm size fraction (KJG) of the KJ SiC separate (Amari et al. 1994). They were deposited from a suspension and pressed into high-purity gold foil with a sapphire window. Prior to RIMS analysis, energy-dispersive X-ray spectroscopy (EDS) mapping was used to locate the 18 SiC grains investigated in this study and those analyzed in a previous study (Stephan et al. 2018), which are from the same sample mount.

2.2. RIMS Analysis

The analytical procedures for the RIMS measurements have been generally described by Stephan et al. (2016). The SiC grains were located with CHILI's integrated scanning electron microscope and then ablated by a 351 nm wavelength desorption laser beam, focused to ~1 µm with a Schwarzschild microscope. The beam intensity was controlled with an active feedback system to keep the desorption rate and therefore the count rate at a low and constant level, so that dead time effects (Stephan et al. 1994) were small and correctable. Light from six Ti:sapphire lasers, individually tuned to specific wavelengths, was collinearized with a three-prism beam combiner, sent through the cloud of neutrals desorbed from the grains, and bounced back through the cloud onto itself. For resonance ionization, we used previously established wavelength schemes for strontium (λ_1 = 460.862 nm, λ_2 = 405.214 nm; Liu et al. 2015), molybdenum (λ_1 = 313.350 nm, λ_2 = 388.337 nm; Barzyk et al. 2007), and barium (λ_1 = 307.247 nm, λ_2 = 883.472 nm; Savina et al. 2003b). Laser wavelengths were kept constant during the entire measurement sessions by using an active feedback system in the Ti:sapphire lasers (Levine et al. 2009; Stephan et al. 2016). Photoions were then separated according to their mass-to-charge ratios in a reflectron-type time-of-flight mass spectrometer and detected with a microchannel plate detector. The time-of-flight spectra were corrected for dead time effects (Stephan et al. 1994).

Standards used to correct for instrumental isotopic fractionation are NIST SRM 855a (aluminum casting alloy 356 with 180 ppm strontium and noncertified, but detectable trace amounts of molybdenum), NIST SRM 1264a (low alloy, high carbon steel with 0.49 wt% molybdenum), and terrestrial $BaTiO_3$. RIMS standards that differ in their chemical and physical properties from the analyzed samples are acceptable, as long as the elements of interest desorb as single atoms, since ionization occurs after the atoms have left the surface. All standards were assumed to be of average terrestrial isotopic composition (Meija et al. 2016), which is a reasonable assumption at precisions of a few parts per thousand (‰). Instrumental mass-dependent isotope fractionation for molybdenum was about –12 ‰/u. In addition, an odd-even effect (Fairbank et al. 1989) was observed for ^{95}Mo and ^{97}Mo, enhancing the sensitivities for these isotopes relative to those with even mass numbers by 21 ‰ and 8 ‰, respectively. Strontium and barium showed similar mass-dependent and mass-independent isotopic fractionation of up to a few tens of ‰. All these effects were corrected for with standards.

2.3. NanoSIMS Analysis

Subsequent to RIMS measurements, residues of all 18 SiC grains were analyzed for carbon, nitrogen, silicon, and sulfur isotopes using the CAMECA NanoSIMS 50 at the Max Planck Institute for Chemistry in Mainz, Germany (Hoppe et al. 2013). A Cs^+ primary ion beam (~1 pA, ~100 nm) was used, and secondary ion images (3×3 to 10×10 μm^2) of $^{12}C^-$, $^{13}C^-$, $^{28}Si^-$, $^{29}Si^-$, and $^{30}Si^-$ were recorded simultaneously. In a second round of analyses, secondary ion images of $^{12}C^{14}N^-$, $^{12}C^{15}N^-$, $^{28}Si^-$, $^{32}S^-$, and $^{34}S^-$ were recorded to determine nitrogen and sulfur isotopic ratios. A synthetic SiC served as a standard to correct for instrumental mass fractionation. Finally, using an O^- beam (Hyperion ion source, ~4 pA, ~100 nm; Hoppe et al. 2018), secondary ion images (5×5 to 8×8 μm^2) of $^{24}Mg^+$, $^{25}Mg^+$, $^{26}Mg^+$, and $^{27}Al^+$ were recorded together with $^{28}Si^+$ in three of the SiC grains to determine $^{26}Al/^{27}Al$ ratios at the time of grain formation. Here, Burma spinel was used as a magnesium isotope standard. The relative sensitivity factor $\varepsilon(Al^+/Mg^+) = 1.56$, required to infer $^{26}Al/^{27}Al$ ratios, was taken from Hoppe et al. (2010). Since NanoSIMS analyses were performed after CHILI measurements on grain residues with very limited material left, magnesium-aluminum analyses could only be performed on a subset of grains, and inferred $(^{26}Al/^{27}Al)_0$ ratios had large statistical errors.

Table 1

Isotope data of 18 presolar silicon carbide grains analyzed with NanoSIMS and CHILI

Grain	Type	$^{12}C/^{13}C$	$^{14}N/^{15}N$	$\delta^{29}Si_{28}$ (‰)	$\delta^{30}Si_{28}$ (‰)	$(^{26}Al/^{27}Al)_0$ (10^{-5})	$\delta^{84}Sr_{86}$ (‰)	$\delta^{87}Sr_{86}$ (‰)	$\delta^{88}Sr_{86}$ (‰)	$\delta^{92}Mo_{96}$ (‰)	$\delta^{94}Mo_{96}$ (‰)	$\delta^{95}Mo_{96}$ (‰)	$\delta^{97}Mo_{96}$ (‰)	$\delta^{98}Mo_{96}$ (‰)	$\delta^{100}Mo_{96}$ (‰)	$\delta^{130}Ba_{136}$ (‰)	$\delta^{132}Ba_{136}$ (‰)	$\delta^{134}Ba_{136}$ (‰)	$\delta^{135}Ba_{136}$ (‰)	$\delta^{137}Ba_{136}$ (‰)	$\delta^{138}Ba_{136}$ (‰)
#a1	MS	53.3±0.2	1356±73	+114±5	+97±6	…	–892±15	–11±14	–84±9	–867±9	–824±13	–530±18	–443±24	–242±22	–866±11	–608±167	–571±190	+100±48	–654±15	–414±19	–346±15
#a13	MS	89.0±0.7	…	+13±6	+12±8	…	–652±92	+88±49	+50±33	–32±6	–23±7	–19±6	–13±7	–14±5	–33±7	–248±142	–474±133	+146±41	–786±10	–492±15	–280±14
#a16	MS	63.6±0.7	378±26	+54±11	+25±14	…	…	…	…	–934±2	–891±3	–601±5	–485±7	–235±7	–928±3	…	…	…	…	…	…
#a17	MS	83.8±0.8	1186±106	+43±13	+37±16	…	…	…	…	–919±3	–880±4	–570±6	–488±9	–229±8	–903±4	…	…	+50±57	–750±15	–470±19	–300±17
#a19	MS	68.6±0.8	1040±155	+62±12	–4±15	…	–839±31	–32±23	–152±14	–729±11	–723±14	–422±18	–380±22	–176±21	–683±15	…	…	–72±69	–572±29	–349±33	–316±25
#a20	MS	49.8±0.4	430±29	+7±11	+19±14	…	…	…	…	–928±2	–881±4	–621±6	–495±9	–259±9	–931±3	…	…	…	…	…	…
#a21	MS	54.3±0.5	1477±178	+81±7	+90±9	…	…	…	…	–151±75	–132±90	–72±78	–25±97	+34±78	+15±99	…	…	…	…	…	…
#a22	MS	70.4±1.0	354±36	+84±16	+60±20	…	…	…	…	–942±2	–896±3	–605±5	–498±7	–241±7	–931±3	…	…	…	…	…	…
#a23	MS	63.5±0.5	515±32	+16±9	+29±12	…	…	…	…	–941±1	–914±2	–549±4	–511±6	–227±6	–903±2	…	…	…	…	…	…
#a24	MS	90.2±1.0	304±14	–16±13	+39±17	…	…	…	…	–887±2	–859±3	–511±5	–475±6	–222±6	–850±3	…	…	–189±259	–607±115	–294±144	–271±113
#a25	MS	37.4±0.2	237±6	+58±11	+58±14	<271	…	…	…	–729±8	–718±11	–411±13	–415±16	–217±15	–716±11	…	…	…	…	…	…
#a26	MS	69.0±0.6	463±49	+56±13	+37±16	…	–875±8	–13±8	–65±5	–800±7	–781±9	–494±11	–404±16	–198±14	–798±9	–796±55	–671±71	+40±28	–665±9	–416±12	–342±9
#a27	MS	71.3±0.9	476±40	+83±11	+53±14	…	…	…	…	–819±9	–812±11	–511±16	–445±20	–204±20	–821±11	…	…	…	…	…	…
#a28	MS	68.7±0.9	543±51	+76±14	+39±17	…	–851±14	–11±13	–130±8	–740±8	–739±9	–442±12	–383±15	–186±14	–737±9	–558±130	–736±113	–90±45	–539±20	–367±21	–344±16
#a29	MS	63.0±0.5	226±4	+71±9	+56±12	142±75	…	…	…	–805±9	–772±12	–531±15	–414±20	–219±19	–777±12	…	…	…	…	…	…
#a30	MS	78.7±0.4	587±57	+53±8	+48±10	…	–906±20	+7±22	–40±14	–842±4	–831±5	–496±7	–442±9	–233±9	–826±5	–750±108	–797±96	–37±46	–696±16	–461±19	–320±17
#a31	MS	53.0±0.1	383±25	+74±5	+68±7	…	…	…	…	–707±24	–638±32	–425±35	–403±43	–228±39	–639±32	…	…	…	…	…	…
#a18	AB2	9.71±0.05	1101±92	–10±12	+3±15	137±21	–756±77	+8±45	–2±30	–698±17	–747±20	–409±26	–400±34	–181±29	–668±23	…	…	–94±74	–648±28	–382±34	–326±28

Notes. Isotope ratios for all elements but carbon, nitrogen, and aluminum are reported as δ-values, defined as $\delta^{i}A_{j} = [(^{i}A/^{j}A)_{grain}/(^{i}A/^{j}A)_{std} - 1] \times 1000$, giving the deviation of an isotope ratio ($^{i}A/^{j}A$) measured in a grain from that isotope ratio measured in a terrestrial standard (std) in parts per thousand (‰). All values are reported with their 1σ uncertainties resulting from counting statistics and, for NanoSIMS data, from reproducibility of the standards. Type "MS" denotes mainstream grains.

3. Results

Table 1 lists isotopic data for 18 presolar SiC grains obtained with NanoSIMS and with CHILI. Sulfur isotopic data are not listed, as they are likely compromised by contamination, as indicated by orders of magnitude higher sulfur concentrations than determined previously for mainstream SiC grains (Hoppe et al. 2015). From their carbon, nitrogen, and silicon isotopes, all but one grain were identified as mainstream grains, with $^{12}C/^{13}C$ ratios between 37 and 90, $^{14}N/^{15}N$ ratios between 230 and 1500, and silicon isotopes following the mainstream correlation trend (e.g., Zinner 2014). Carbon, nitrogen, and silicon data are compared with literature data in Figure 2.

One grain (#a18) has a $^{12}C/^{13}C$ ratio of 9.7, a $^{14}N/^{15}N$ ratio of ~1100, and silicon isotope ratios that are nearly solar. The grain was therefore classified as an AB grain, as this type has $^{12}C/^{13}C$ ratios below 10. Following the scheme introduced by Liu et al. (2017a, b), this grain is an AB2 grain, because it has a high $^{14}N/^{15}N$ ratio relative to the Solar System (Figure 2).

The inferred $(^{26}Al/^{27}Al)_0$ ratios for one mainstream and the AB2 grain were 1.4×10^{-3}; and for one mainstream grain, only an upper limit of $<2.7\times10^{-3}$ could be determined. These values are typical for such grains (see, e.g., Figure 5 in Zinner 2014) and are therefore not discussed here any further.

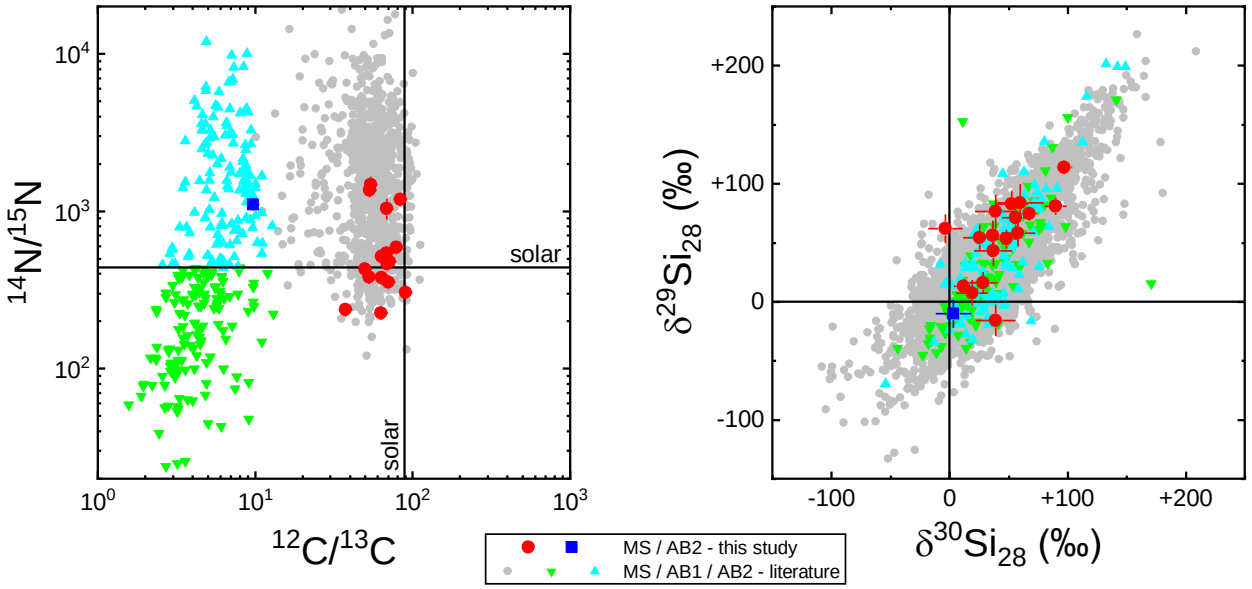

Figure 2. Carbon, nitrogen (left), and silicon (right) isotope ratios of individual presolar SiC grains measured in this study compared to literature data for mainstream (MS) and for AB1 and AB2 grains (Alexander 1993; Hoppe et al. 1994, 1996, 2010, 2012; Huss et al. 1997; Amari et al. 2001; Nittler & Alexander 2003; Nittler & Hoppe 2005; Marhas et al. 2008; Xu et al. 2015; Liu et al. 2016, 2017a, b, 2018b), excluding silicon literature data with uncertainties (1σ) >20 ‰. Error bars for literature data are not shown. Error bars for grains from this study are 1σ.

3.1. Strontium

Strontium isotopes were reliably measured in six of the mainstream grains and the AB2 grain; concentrations in the remaining grains were too low to obtain meaningful isotope ratios. The results (Table 1 and Figure 3) show the expected strong depletion of ^{84}Sr relative to ^{86}Sr and solar abundances, which is typical for such grains and reflects that the *p*-process isotope is not made in the *s*-process. Relative to ^{86}Sr and solar abundances, ^{87}Sr concentrations are all within 2σ of solar, whereas ^{88}Sr/^{86}Sr ratios are solar to subsolar (down to $\delta^{88}Sr_{86}$ = –152 ‰). These results are fully in line with previous observations in mainstream grains (e.g., Nicolussi et al. 1998b; Liu et al. 2015; Stephan et al. 2018). Both ^{86}Sr and ^{87}Sr are *s*-process-only isotopes, whereas ^{88}Sr, although dominated by *s*-process nucleosynthesis, is a mixed *s*- and *r*-process isotope. The observed strontium isotope pattern therefore strongly points towards the *s*-process as having occurred in the grains' parent stars.

The AB2 grain showed the same *s*-process pattern in strontium isotopes as observed for the mainstream grains, including a strong depletion in ^{84}Sr/^{86}Sr relative to solar. This is different from a previous report on three AB2 grains, for which ^{84}Sr data are available (Liu et al. 2017b). Their AB2 grains showed close-to-normal ^{84}Sr/^{87}Sr ratios, which might have been caused by contamination with Solar System material (Liu et al. normalized their strontium data to ^{87}Sr due to an unresolved mass interference at ^{86}Sr).

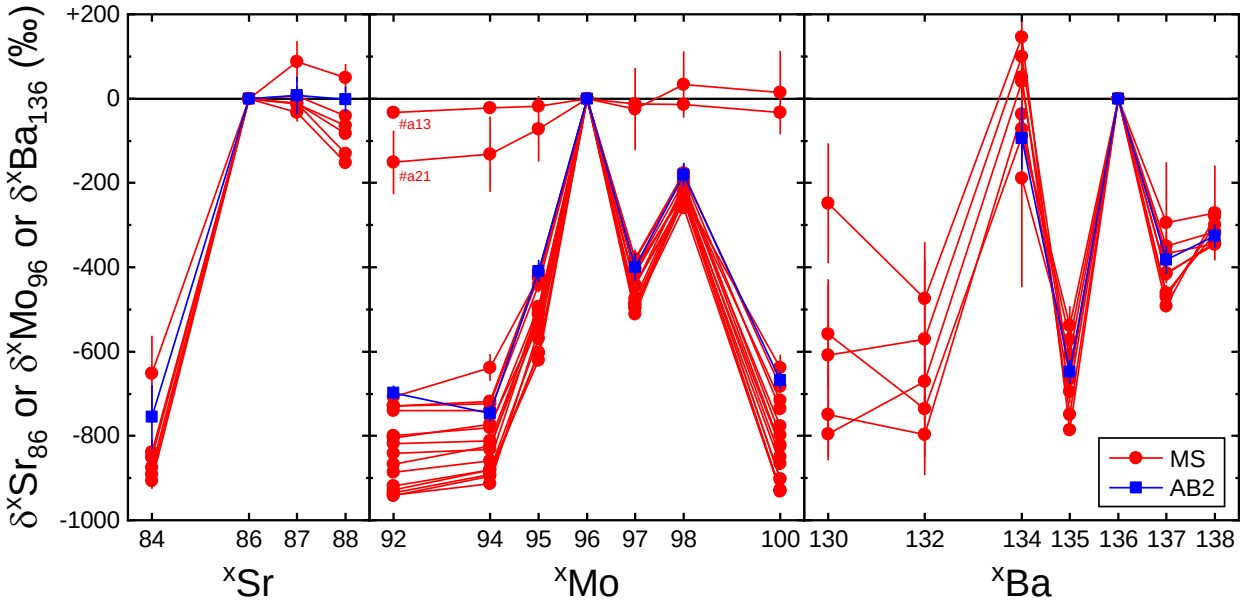

Figure 3. Strontium, molybdenum, and barium isotopes for 17 mainstream (MS) grains and one AB2 grain show the typical *s*-process patterns with strong depletions in *p*- and *r*-process isotopes and intermediate depletions in mixed *s*- and *r*-process isotopes compared to the *s*-process-only isotopes ^{86}Sr, ^{96}Mo, and ^{136}Ba.

3.2. Barium

Barium isotopes (Table 1 and Figure 3) from the mainstream grains also show the expected *s*-process pattern. The two *p*-process isotopes ^{130}Ba and ^{132}Ba, which, due to their low abundance, could only be measured in five mainstream grains, showed a strong depletion relative to ^{136}Ba and solar abundances. Other barium isotopes were also reliably measured in these five and three more mainstream grains. All eight mainstream grains show rather normal ^{134}Ba and strong depletions of ^{135}Ba, ^{137}Ba, and ^{138}Ba relative to ^{136}Ba and solar abundances. Again, this is in line with previous observations in mainstream grains (e.g., Liu et al. 2015; Stephan et al. 2018) and can be explained by the *s*-process-only origin of ^{134}Ba and ^{136}Ba and the mixed *s*- and *r*-process nature of ^{135}Ba, ^{137}Ba, and ^{138}Ba.

The AB2 grain again showed the same *s*-process pattern in barium isotopes as observed for the mainstream grains. This is different from solar barium isotope ratios found in the one AB2 grain, for which barium isotope data have been published in the literature (Liu et al. 2017b) and which might have suffered from contamination.

3.3. Molybdenum

Molybdenum isotopes, which were reliably detected in all grains, show the typical *s*-process pattern for most grains, including the AB2 grain. Two grains, #a13 and #a21, are close to solar in composition (Table 1 and Figure 3). Figure 4 shows the data as three-isotope plots together with RIMS data from the literature (Nicolussi et al. 1998a; Barzyk et al. 2007; Liu et al. 2017b). Compared to those results, our data show a significantly improved measurement precision, as can be seen from the generally smaller errors and narrower distribution of our data points around the regression lines (Figure 4). These lines are weighted, linear regressions through the data points from the 17 mainstream grains from this study and have been calculated using the method of Mahon (1996), which is an updated and corrected "York" regression (York 1969). Correlated errors resulting from the common normalizing isotope ^{96}Mo were taken into account.

For all regression lines, the goodness of fit was determined by calculating mean square weighted deviation (MSWD) values, also known as reduced χ^2 values, which are given in Figure 4. MSWD values of 1.0 and 1.7, respectively, for the $\delta^{97}Mo_{96}$ and $\delta^{98}Mo_{96}$ versus $\delta^{92}Mo_{96}$ linear regressions are both within a 95 % confidence interval of [0.417, 1.833], calculated from the χ^2 distribution for a single comparison of 17 data points (15 degrees of freedom). One should be aware that an MSWD value calculated from experimental data and their uncertainties is itself a number that is subject to statistical fluctuations. For a large sample, the MSWD converges towards the "true" value, which can be used to determine if a scatter can be explained by the measurement uncertainties of the individual data points. It is therefore useful to calculate confidence intervals for MSWD values depending on a given sample size to determine the significance of an MSWD value deviating from unity. Using a 95 % confidence interval is the conventional approach. While the MSWD value of 1.0 for the $\delta^{97}Mo_{96}$ versus $\delta^{92}Mo_{96}$ linear regressions clearly suggests that there was no scatter detected beyond what is explained by the measurement uncertainties, the MSWD of 1.7 for $\delta^{98}Mo_{96}$ versus $\delta^{92}Mo_{96}$ is marginal. Therefore, we cannot exclude that there is some extra scatter in the $\delta^{98}Mo_{96}$ versus $\delta^{92}Mo_{96}$ data beyond measurement uncertainties. However, MSWD values for $\delta^{94}Mo_{96}$, $\delta^{95}Mo_{96}$, and $\delta^{100}Mo_{96}$ versus $\delta^{92}Mo_{96}$ of 4.7, 16.3, and 9.9, respectively, are all clearly above the upper bound of the 95 %

confidence interval, meaning that there is unambiguous scatter beyond measurement uncertainties.

While MSWD values significantly below the lower bound of the 95 % confidence interval can only be explained by overestimated uncertainties, MSWD values above the upper bound of the confidence interval (i.e., the data scatter about the regression line by more than is expected from the uncertainties of the individual data points), like in these three cases, can arise for two reasons. Either uncertainties are significantly underestimated, or the applied fit does not fully explain the data distribution. There is no methodological reason related to our RIMS analyses why only three of the six measured molybdenum isotope ratios should have significantly underestimated uncertainties, while the uncertainties for the other isotope ratios are within the 95 % confidence interval. Therefore, it can be concluded that the observed trends in $\delta^{94}Mo_{96}$, $\delta^{95}Mo_{96}$, and $\delta^{100}Mo_{96}$ versus $\delta^{92}Mo_{96}$ are not fully described by the linear regressions shown in Figure 4 but need further explanation accounting for deviations from these fits.

It should be emphasized that the high MSWD values reported in this study are not due to underestimates of measurement uncertainties in the data; instead, they represent a measure for the true scatter about the regression lines that is caused by nucleosynthetic effects to be described later. Thus, for the reported errors of the extrapolated values at $\delta^{92}Mo_{96} = 0$ ‰ and $\delta^{92}Mo_{96} = -1000$ ‰, we multiplied the uncertainties calculated for the regressions according to Mahon (1996) with the square root of the MSWD value (when this value is greater than unity) to reflect the uncertainty resulting from the scatter, as it is not part of the original Mahon (1996) fit. This is equivalent to multiplying the uncertainty for each data point by the square root of the MSWD for the regression, which does not change the slopes or intercepts, but increases the uncertainties of the slopes and intercepts.

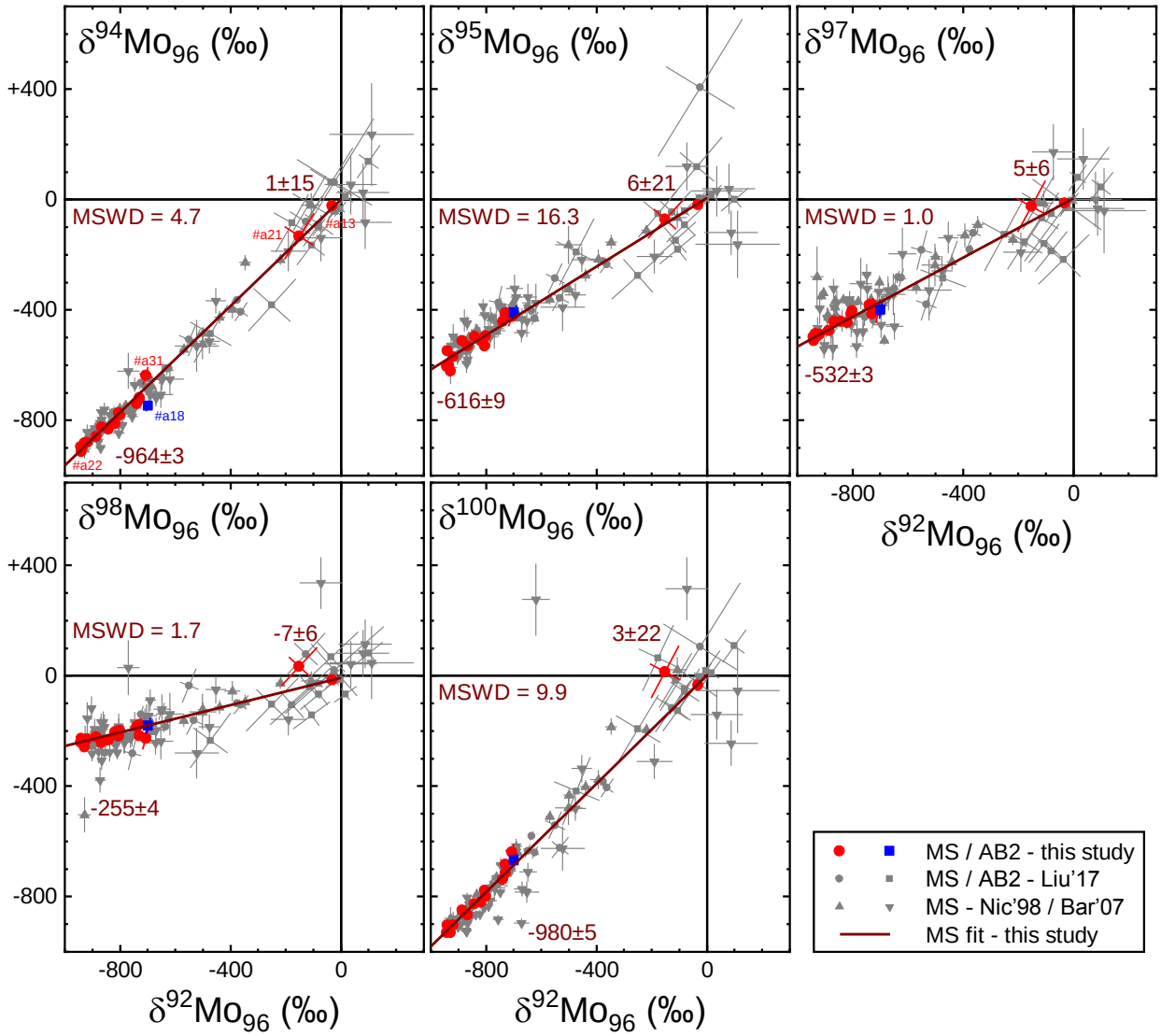

Figure 4. Molybdenum isotope data for 18 presolar SiC grains from this study in comparison with literature data for mainstream (MS) and AB2 grains (Nic'98 = Nicolussi et al. 1998a; Bar'07 = Barzyk et al. 2007; Liu'17 = Liu et al. 2017b). The shown fits represent weighted, linear regression lines (Mahon 1996) through the mainstream grain data from this study only, not forced through the origin. The numbers at both ends of each regression line give the intercepts for $\delta^{i}Mo_{96}$ at $\delta^{92}Mo_{96} = -1000‰$ and $\delta^{92}Mo_{96} = 0‰$, respectively, and their 1σ uncertainties resulting from individual uncertainties of the data points and their scatter. MSWD values as a measure for the goodness of fit are also shown for each regression. For data from this study and from Liu et al. (2017b), error correlation has been taken into account and 1σ error bars shown are therefore not parallel to the plot axes. Error bars for other literature data are 1σ as well. For data points toward the left edges of the graphs, symbols are much larger than their error bars.

As can be seen in Figure 4, all regression lines, within statistical errors, pass through the origins, $\delta^{i}Mo_{96} = 0$ ‰ at $\delta^{92}Mo_{96} = 0$ ‰. One might argue that this is mainly due to including the data from grain #a13, which has a molybdenum composition rather close to solar and small uncertainties (Table 1, Figure 3). This grain shows large depletions in the *p*- and *r*-process contributions to strontium and barium isotopes (Table 1), and one would expect similar depletions in *p*- and *r*-process molybdenum. Nevertheless, $\delta^{i}Mo_{96}$ values are all close to zero for grain #a13 (Table 1), which can probably only be explained by significant contamination with solar molybdenum. However, since grain #a13 is still clearly anomalous, with isotope ratios 2–5 standard deviations from normal, we decided not to eliminate it from these calculations. Although eliminating data from grain #a13 from the fits would have some effect on the intercepts, uncertainties of the intercepts at $\delta^{92}Mo_{96} = 0$ ‰ would, at the same time, increase significantly. Another option would be to consider all molybdenum literature data for mainstream SiC grains shown in Figure 4 in the regressions, diminishing the influence of a single measurement on the entire data set. In that case, all extrapolated values for $\delta^{92}Mo_{96}$ at 0 ‰ would still be $\delta^{i}Mo_{96} = 0$ ‰ within the statistical uncertainty.

Grain #a21, which is also close to solar in its molybdenum composition (Table 1, Figure 3) and which shows large absolute deviations from some regression lines in Figure 4, does not play any significant role in these calculations. For this grain, we detected the by far smallest number of molybdenum atoms of all analyzed grains and therefore obtained the largest uncertainties, so that it had no influence on the weighted linear regressions. Also the MSWD values depend very little on this specific grain.

The other ends of the regression lines are shown as intercepts at $\delta^{92}Mo_{96} = -1000$ ‰ in Figure 4. Since ^{92}Mo is a *p*-process-only isotope, these intercepts could be interpreted as being representative of the pure *s*-process endmember isotope ratios in these mainstream grains (Nicolussi et al. 1998a).

While linear regressions from all values from mainstream grains shown in Figure 4, including those from literature, do not significantly change the observed trends, there seem to be some significant differences between the various data sets. In particular, the intercepts for $\delta^{95}Mo_{96}$ and $\delta^{97}Mo_{96}$ at $\delta^{92}Mo_{96} = -1000$ ‰ calculated from the data by Nicolussi et al. (1998a), and to some extent also by Barzyk et al. (2007), would be significantly higher, by up to 82 ‰, than the values reported here. Also, the scatter about the regression for $\delta^{97}Mo_{96}$ versus $\delta^{92}Mo_{96}$ seems to be much broader in those data sets. The broader distribution and the higher $\delta^{95}Mo_{96}$ and $\delta^{97}Mo_{96}$ intercepts calculated from the literature data could, however, in part be explained by less-controlled measurement conditions during resonance ionization. For example, drifting laser wavelengths during those measurements could have caused an odd-even effect favoring the ionization of the isotopes with odd mass numbers. During our CHILI measurements, laser wavelengths were kept constant, and the ionization process was well saturated, leading only to very minor odd-even effects that were consistent throughout our measurements and that we corrected for with standards. The literature data by Nicolussi et al. (1998a) and Barzyk et al. (2007) were taken with an older generation RIMS instrument prior to introducing the active feedback system controlling ionization laser wavelength stabilities. The analyses reported by Liu et al. (2017b), on the other hand, suffered from much larger statistical uncertainties than our new data due to low count rates. Intensive presputtering of those grains during prior NanoSIMS measurements consumed major fractions of those grains and left only little material for the RIMS analyses. In addition, some contamination issues caused mass interferences from nonresonant

ionization of molecules. We are therefore confident that the values presented here are more accurate than any literature data published previously and, for the following discussion, use mainly our new mainstream grain results.

Among the SiC grains analyzed in the present study is one AB2 grain (#a18), for which most isotopes relative to ^{96}Mo show results in agreement with the trends observed for the mainstream grains (Figure 4). The only significant difference was found in $\delta^{94}Mo_{96}$ versus $\delta^{92}Mo_{96}$, where the AB2 grain plots below the mainstream regression line (Figure 4). Unfortunately, the molybdenum literature data available for other AB2 grains (Liu et al. 2017b) suffer from relatively large uncertainties, so it is not clear that this difference is characteristic of AB2 grains in general.

4. Discussion

4.1. Mixing Nucleosynthetic Products

The isotopic compositions of presolar grains that formed around dying stars and made their way into primitive meteorites, in general, reflect a combination of three possible sources: (1) atoms that initially formed the parent stars and that were still present in their unprocessed envelopes at the beginning of the AGB phase; (2) atoms newly synthesized in those stars; and (3) atoms with solar isotopic composition from the protosolar cloud, the host meteorite's parent body, or from contamination during chemical extraction and handling of grains in the laboratory. Solar System material itself is a complex mixture of atoms formed in various nucleosynthetic processes under a variety of conditions in many different stars.

While solar composition should represent the isotopic composition of the molecular cloud from which the Solar System originated some 4.6 Ga years ago, the parent stars of presolar grains formed earlier, from interstellar matter that could have had different isotopic composition. Low-mass AGB stars, like those from which our mainstream SiC grains probably originated, have typical lifetimes of 0.3–3 Ga. Furthermore, based on their cosmogenic helium, neon, and lithium contents, mainstream presolar SiC grains have typical interstellar residence times of 3.9±1.6 Ma to 3.2±2.3 Ga, with most <500 Ma (Gyngard et al. 2009; Heck et al. 2009, 2019), before being incorporated into the forming Solar System. Therefore, we estimate that the parent stars of our grains formed 0.3–6 Ga before the formation of the Solar System. Due to galactic chemical evolution and/or heterogeneities in the interstellar medium, one would expect that the initial isotopic composition of those parent stars should be at least somewhat different from solar. One might get some idea of the expected spread by looking at the variation of ratios between an *s*-process-dominated element like, e.g., barium (85 % *s*-process; Bisterzo et al. 2014) and an *r*-process-dominated element like europium (94 % *r*-process; Bisterzo et al. 2011) depending on metallicity. The ratio between these elements varies by a factor of two among individual stars with near-solar metallicity (e.g., Battistini, & Bensby 2016; Bisterzo et al. 2017). A similar variability should therefore also be expected for initial stellar isotope ratios between *s*- and *r*-process-only isotopes like ^{96}Mo and ^{100}Mo.

The molybdenum isotope data for the mainstream SiC grains investigated, however, can be almost entirely explained by a simple two-component mixing model. One endmember is within a few ‰ of the solar composition; the other endmember is given by the *s*-process. We are

therefore confident that the observed trends in Figure 4 are best described as mixing lines with a solar endmember, and, in Table 2, we forced all regression lines through solar values at (0,0). Forcing all regression lines through solar composition had little effect on the calculated extrapolations for the *s*-process, as could be seen from nearly identical intercepts at $\delta^{92}Mo_{96} = -1000$ ‰ in Figure 4 and in Table 2, and the similar MSWD values. The 95 % confidence interval for MSWD values of a single forced fit is [0.432, 1.803]. As in Figure 4, uncertainties in the intercepts at $\delta^{92}Mo_{96} = -1000$ ‰ are multiplied by the square root of the MSWD, so that the uncertainties reflect both measurement uncertainties and actual scatter of the data. In the following, we will regard the values obtained from the forced fit ($\delta^{i}Mo_{96,s}$) as our best estimate for average *s*-process composition.

Using the average *s*-process composition and the isotopic composition of the Solar System (last column in Table 2; Meija et al. 2016) and assuming that ^{96}Mo is solely produced by the *s*-process, we can calculate the contributions of the *p*- and *r*-processes to the individual molybdenum isotopes. From this simplified approach, the solar composition of molybdenum could be seen as a combination of 45.9 % *s*-process, 30.6 % *r*-process, and 23.5 % *p*-process molybdenum with compositions for each of the three components given in Table 2 (columns 4–6).

The observation that one endmember is indistinguishable from Solar System composition is either profound or trivial. The trivial explanation is that we observe a mixture between pure *s*-process molybdenum and Solar System material in these grains and that the initial composition of the individual parent stars played no significant role. While there is huge production of *s*-process isotopes in the ^{13}C pocket of low-mass AGB stars, subsequent dilution with unprocessed stellar matter in the envelope of the AGB star prior to SiC grain condensation should have played a role.

This leads to the other, more intricate explanation that requires the initial molybdenum isotopic composition of each parent star to lie in every single plot shown in Figure 4 somewhere close to respective regression line defined by the *s*-process endmember and the solar composition. At first sight, this might seem improbable, but for the initial composition of all mainstream grain parent stars to lie on the regression lines in Figure 4, their molybdenum must consist of a mixture of *s*-, *r*-, and *p*-process components with isotopic abundances as shown in columns 4–6 in Table 2, and the ratio between the *p*- and *r*-process components would have to be $Mo_p/Mo_r = 0.767 \pm 0.004$, the ratio we derived for the Solar System. It is important to emphasize here that a constant Mo_s/Mo_{r+p} ratio would not be required as changing this ratio would move data points only along the regression lines in Figure 4. Observing an association between *r*- and *p*-process isotopes is not new in presolar grain research. Presolar diamond, the most abundant and first-isolated presolar grain species (Lewis et al. 1987), contains xenon-HL, a xenon component enriched in *r*- and *p*-process xenon isotopes (Reynolds & Turner 1964; Lewis et al. 1975), which has been attributed to a supernova origin (see Zinner 2014 and references therein). However, due to the small grain size of presolar diamonds, ~2.6 nm on average (e.g., Zinner 2014), and its low concentration, xenon-HL can only be detected by analyzing a huge number of grains, which therefore only provides an average composition probably from a large number of parent stars. Attempts to separate xenon-HL into distinct *p*- and *r*-process components have failed so far (e.g., Meshik et al. 2001). Unfortunately, there are no constraints on the ratio of *p*- to *r*-process isotopes from stellar spectroscopy, because there are no elements whose nucleosynthetic production is dominated by the *p*-process.

Table 2
Results from weighted, linear regression calculations for 17 mainstream SiC grains

^{i}Mo	$\delta^{i}M_{96,s}$ (‰)	MSWD	$^{i}Mo_{s}/Mo_{s}$ (%)	$^{i}Mo_{r}/Mo_{r}$ (%)	$^{i}Mo_{p}/Mo_{p}$ (%)	$^{i}Mo_{\odot}/Mo_{\odot}$ (%)
^{92}Mo	–1000	–	0	0	62.3	14.649
^{94}Mo	–964±3	4.4	0.73±0.06	0	37.7	9.187
^{95}Mo	–615±8	15.4	13.30±0.25	31.9	0	15.873
^{96}Mo	–	–	36.34±0.13	0	0	16.673
^{97}Mo	–532±3	1.0	9.78±0.06	16.6	0	9.582
^{98}Mo	–256±4	1.8	39.42±0.17	20.3	0	24.292
^{100}Mo	–980±4	9.3	0.43±0.09	31.2	0	9.744

Notes. The first column gives the molybdenum isotope. The second column gives the intercepts at $\delta^{92}Mo_{96}$ = –1000 ‰ for regression lines like those shown in Figure 4 but forced through the origin at (0,0), i.e., solar isotope ratios. These intercepts are interpreted as the average *s*-process endmember composition, hence the notation $\delta^{i}Mo_{96,s}$. The third column gives the mean square weighted deviation (MSWD) of the data points from the forced fit for each isotope, which describes the goodness of fit and represents a measure for the scatter about the regression line that is caused by nucleosynthetic effects. The abundances are then renormalized to 100 % in the fourth column to show the molybdenum isotopic abundances in atomic % for the *s*-process. Attributing the Solar System abundances (last column; according to Meija et al. 2016) to a simple mixture of *s*-, *r*-, and *p*-process, columns five and six give the respective isotopic abundances for the *r*- and *p*-processes. Errors given in columns two and four are 1σ.

For molybdenum, however, there are no presolar grains known that would represent the complementary *r*- and *p*-process endmember, opposite from the *s*-process endmember, that would account for the solar composition, although tiny depletions of *s*-process molybdenum have been observed in bulk samples and leachates of primitive meteorites (Dauphas et al. 2002; Burkhardt et al. 2011, 2012; Budde et al. 2016, 2018). Presolar SiC grains of type X, which are attributed to Type II supernovae, show enrichments of mixed *s*- and *r*-process isotopes ^{95}Mo and ^{97}Mo, but no equivalent enrichment for the *r*-process-only isotope ^{100}Mo and also no enrichment in *p*-process isotopes (Pellin et al. 2006). Therefore, X grain composition cannot serve as the counterpart to the *s*-process in forming the Solar System molybdenum composition. Their composition could, however, be explained by a neutron burst component that is quite distinctive from the *s*-, *r*-, and *p*-processes (Meyer et al. 2000) or by neutrino-driven winds (Hoffman et al. 1996; Farouqi et al. 2009; Bliss et al. 2018).

Nevertheless, taking into account that mainstream SiC grains are expected to come from a large number of different AGB stars, in order to explain their broad range in silicon isotopic compositions (see Figure 2), but also form mixing lines in molybdenum three-isotope plots, the observations can best be explained by assuming a fixed ratio of Mo_{p}/Mo_{r} = 0.767 for the grains' parent stars. It is intriguing that even for non-mainstream grains like the AB2 grain in this study but also AB1, AB2, Y, and Z grains from previous studies (Liu et al. 2017b; Liu et al. 2018b; Liu et al. 2019) all show molybdenum isotope ratios that are indistinguishable from the mixing lines

shown in Figure 4. It could therefore be deduced that *r*- and *p*-process isotopes must either have the same stellar sources or are at least produced at highly correlated rates.

In order to explain the trend in silicon isotopes observed for mainstream grains (Figure 2), several explanations have been given (see Zinner 2014 and references therein). Depending on whether this trend reflects galactic chemical evolution (Gallino et al. 1994; Clayton & Timmes 1997), mixing of different regions of the Galaxy (Clayton 1997), or a merger of the Milky Way with a satellite galaxy (Clayton 2003), a fixed Mo_p/Mo_r ratio could be explained by *r*- and *p*-processes being linked together at a fixed rate over some time (0.3–6 Ga) and perhaps space in the Galaxy and beyond.

Stellar models used to describe *s*-process nucleosynthesis in AGB stars often show trajectories in molybdenum three-isotope plots that are similar to the linear regressions in Figure 4 and that go through solar composition (e.g., Lugaro et al. 2003). However, this is not surprising since those models assume solar initial isotopic composition for most elements (Lugaro et al. 2003), forcing trend lines through solar, and then simply adding *s*-process material from consecutive thermal pulses (see below). While it seems adequate to assume solar initial isotope compositions as long as no coherent model for the evolution of those isotope ratios during galactic history exists, an agreement of grain data with such model trends should not be used as a proof for grain formation along those model trajectories. If just the Mo_p/Mo_r ratio was fixed, the starting point for each star could be anywhere along the regression lines and contamination with solar material could have moved a grain's composition from its initial position along the line towards solar.

Since contamination has been demonstrated to occur in some grains (e.g., Barzyk et al. 2007, and also grain #a13 of this work) and cannot be excluded for other grains, it seems most plausible to interpret the regression lines in Figure 4 as mixing lines between *s*-process molybdenum, Solar System contamination, and the parent star's initial composition, lying on the very same lines as defined by the other two components. It has been suggested that mainstream grains that have $\delta^{92}Mo_{96}$, $\delta^{94}Mo_{96}$, and $\delta^{100}Mo_{96}$ all below –600 ‰ should be considered as free of contamination (Nicolussi et al. 1998a; Barzyk et al. 2007). However, considering all molybdenum data available for mainstream grains (Figure 4), such a distinction seems arbitrary. And even if such bimodality would exist, it could be simply due to a bimodality of molybdenum concentrations making the grains more or less prone but not immune to contamination. Molybdenum carbide, which has been observed in presolar graphite grains and could have condensed prior to SiC (Bernatowicz et al. 1996), being present in some SiC grains and absent in others, could easily cause such bimodality.

However, what remains unexplained by the simple mixing model are the deviations from the linear fits that cause MSWD values to lie significantly outside their respective confidence intervals. Variability around mixing lines could in principle be explained by variations in either endmember or by adding variable contributions from a third component that could also be variable in its composition. Variability in Solar System composition can be excluded because the total variation in molybdenum isotopic composition among bulk meteorites is less than 1 ‰ (Kruijer et al. 2017). While variable contributions from the third component, the unprocessed envelope of the grains' parent star, could in general not be excluded as being responsible for the deviations from the regression lines, it seems rather unlikely that such contributions would only affect three of the five distributions in Figure 4. Any deviation from a constant Mo_p/Mo_r ratio should be detectable, although to different extents, as variations in $\delta^{95}Mo_{96}$, $\delta^{97}Mo_{96}$, $\delta^{98}Mo_{96}$,

and $\delta^{100}Mo_{96}$ versus $\delta^{92}Mo_{96}$. In particular, the effects to $\delta^{95}Mo_{96}$, where we observe the largest MSWD (15.4), and to $\delta^{97}Mo_{96}$, where MSWD = 1, should be similar.

The only plausible explanation therefore is that ^{94}Mo, ^{95}Mo, and ^{100}Mo production in the grains' parent stars cannot be explained by a single *s*-process producing fixed abundances for those isotopes relative to ^{96}Mo. Instead, there must be variations in conditions during *s*-process nucleosynthesis causing these deviations from the mixing lines, which are reflected in the rather large ranges for inferred *s*-process values for these isotopes shown in Figure 5. The values shown there were calculated by extrapolating *s*-process isotope abundances for individual grains to $\delta^{92}Mo_{96}$ = –1000 ‰ with solar ratios as the other endmember. These differences between individual grains are only clearly visible in the new data set from this study. Measurement uncertainties in the literature values (Nicolussi et al. 1998a; Barzyk et al. 2007; Liu et al. 2017b) are in most cases so large that they cannot be used to draw such a detailed picture of variations in *s*-process pathways.

Also, only the new, high precision data allow a search for correlations between *s*-process data extrapolated from individual grains (Figure 6). While $\delta^{97}Mo_{96,s}$ and $\delta^{98}Mo_{96,s}$ showed no significant variations, the variations in $\delta^{95}Mo_{96,s}$ and $\delta^{94}Mo_{96,s}$ are anticorrelated, and the variations in $\delta^{95}Mo_{96,s}$ and $\delta^{100}Mo_{96,s}$ are correlated to each other. For a better understanding of the variations and their relation to each other, one needs to take a closer look at *s*-process nucleosynthesis.

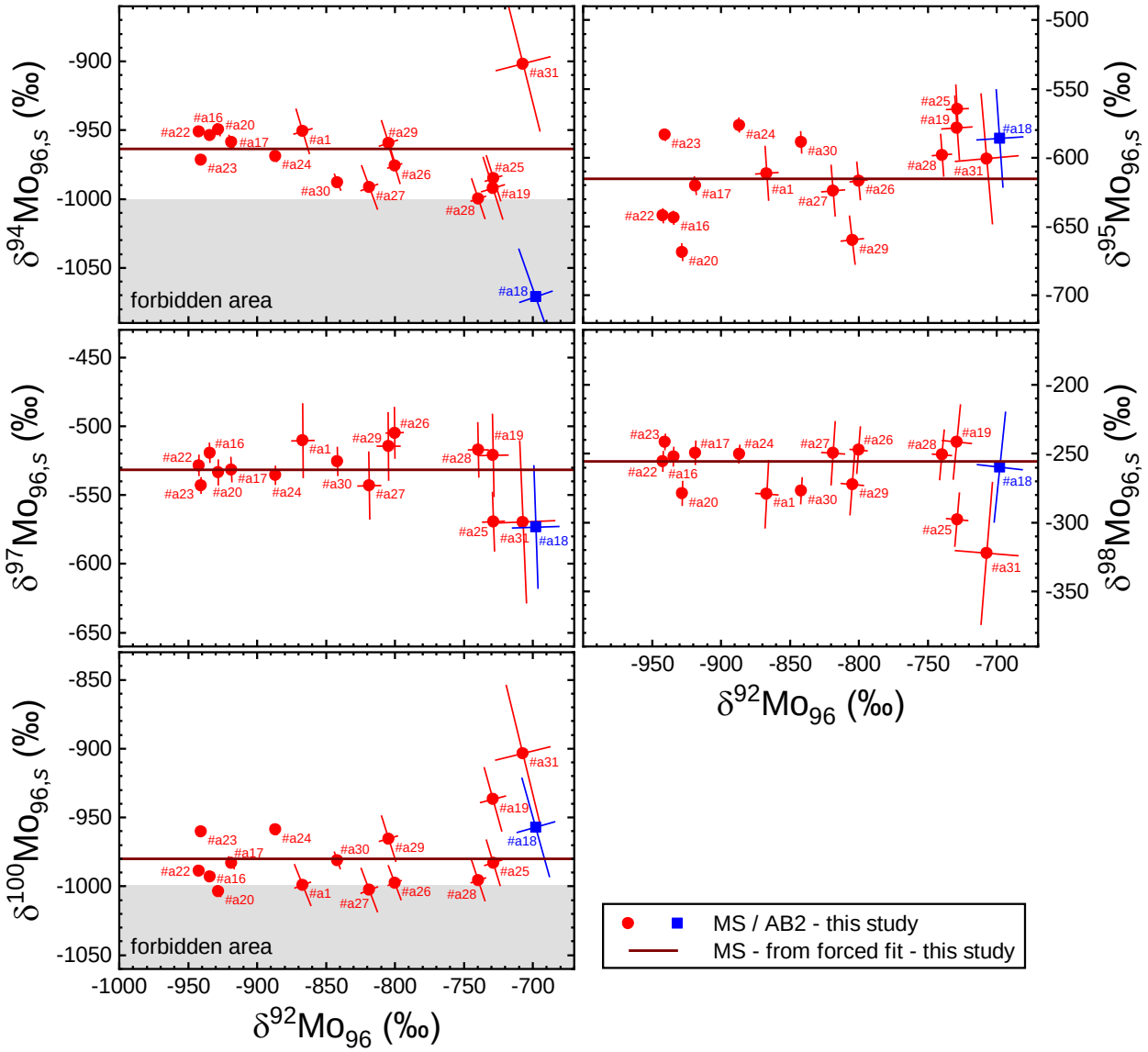

Figure 5. Results from calculating *s*-process isotope abundances for individual grains by extrapolating each individual measurement to $\delta^{92}Mo_{96}$ = –1000 ‰ with solar ratios as the other endmembers. The horizontal lines show the extrapolated values from all mainstream grains from this study (second column in Table 2). For lower $\delta^{92}Mo_{96}$ (closer to –1000 ‰), the 1σ error bars shown get much smaller not only because the measurement uncertainty is smaller but also because these values are not extrapolated as far in $\delta^{92}Mo_{96}$. Delta values below –1000 ‰ are impossible, as they imply negative concentrations, but all data from the "forbidden area" are within 2σ consistent with values above –1000 ‰. Data for grains #a13 and #a21 are not shown here since, due to their $\delta^{92}Mo_{96}$ values close to solar, extrapolated $\delta^{i}Mo_{96,s}$ values have uncertainties of several hundreds of ‰.

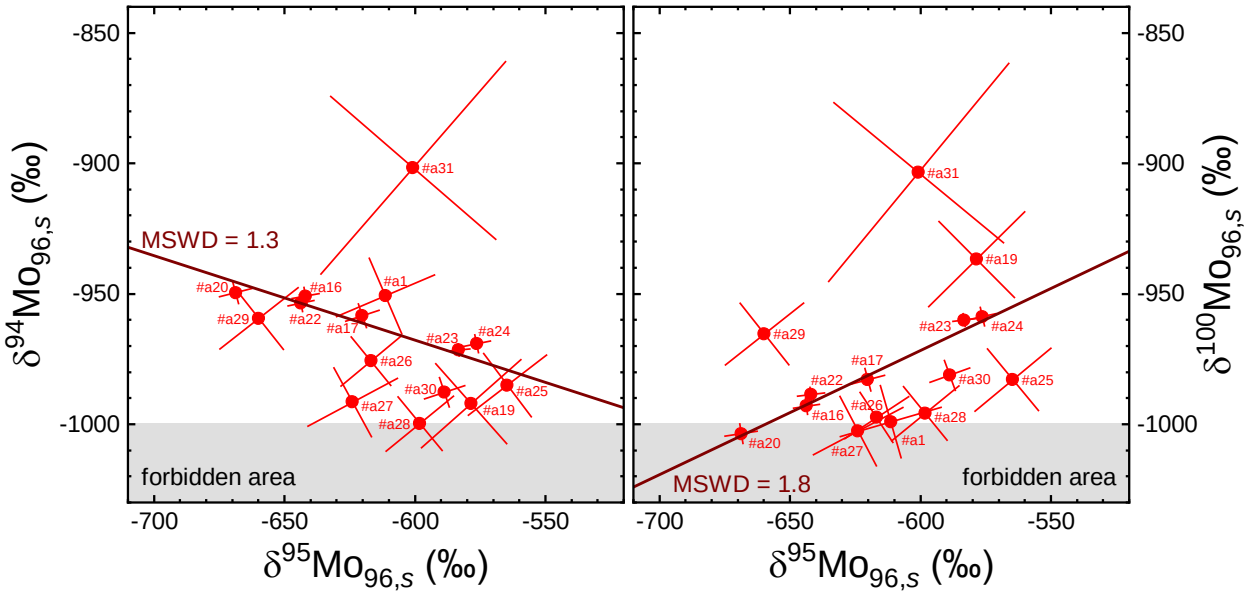

Figure 6. Plotting *s*-process isotope ratios extrapolated from individual grains, as in Figure 5, against each other, shows a negative correlation between $\delta^{95}Mo_{96,s}$ and $\delta^{94}Mo_{96,s}$ and a positive correlation between $\delta^{95}Mo_{96,s}$ and $\delta^{100}Mo_{96,s}$. The regression lines very much depend on the seven data points (#a16, #a17, #a20, #a22, #a23, #a24, and #a30) with the smallest uncertainties (error bars are 1σ) but are calculated by taking into account all mainstream grain data from this study, including data for #a13 and #a21, which have values outside the plotted range and error bars covering several hundreds of ‰, but do not affect the results. The MSWD values close to unity suggest that these trends are real and require explanation.

4.2. The s-Process in AGB Stars

The *s*-process in low-mass AGB stars is expected to occur in thermal pulses in the so-called helium intershell, a region between the hydrogen-rich convective envelope and the carbon-oxygen core, when neutrons are released by two different reactions. Most of the time, the star produces energy by hydrogen burning at the base of the convective envelope, gradually increasing the mass and temperature of the radiative helium intershell. Every few tens of thousands of years, high enough temperature is reached to drive the triple-α reaction at the base of the helium intershell for a few years, causing it to convect and expand in a so-called thermal pulse (TP), which shuts down hydrogen burning temporarily. The first reaction, $^{13}C(\alpha, n)^{16}O$, occurs at temperatures up to 9×10^7 K producing a neutron density of about 10^7 cm^{-3} for up to 10^4 a in a region within the helium intershell called the ^{13}C pocket, which gets diluted in the subsequent TP with material from the rest of the helium intershell that has not received a neutron irradiation. The second reaction, $^{22}Ne(\alpha, n)^{25}Mg$, is marginally activated for a few years during TPs at a temperature of 3×10^8 K, producing a peak neutron density of about 5×10^9 cm^{-3}, and covers almost the entire helium intershell. After the TP ends, the convective envelope can reach into the He intershell and, in a process called third dredge-up (TDU), transfers some newly synthesized ^{12}C and *s*-process material into the stellar envelope. After a few TPs, the envelope reaches C/O>1, and SiC grains can condense. Further details are described in the literature (e.g., Busso et al. 1999; Lugaro et al. 2003, 2014; Straniero et al. 2006; Cristallo et al. 2009; Liu et al. 2014a, 2018a).

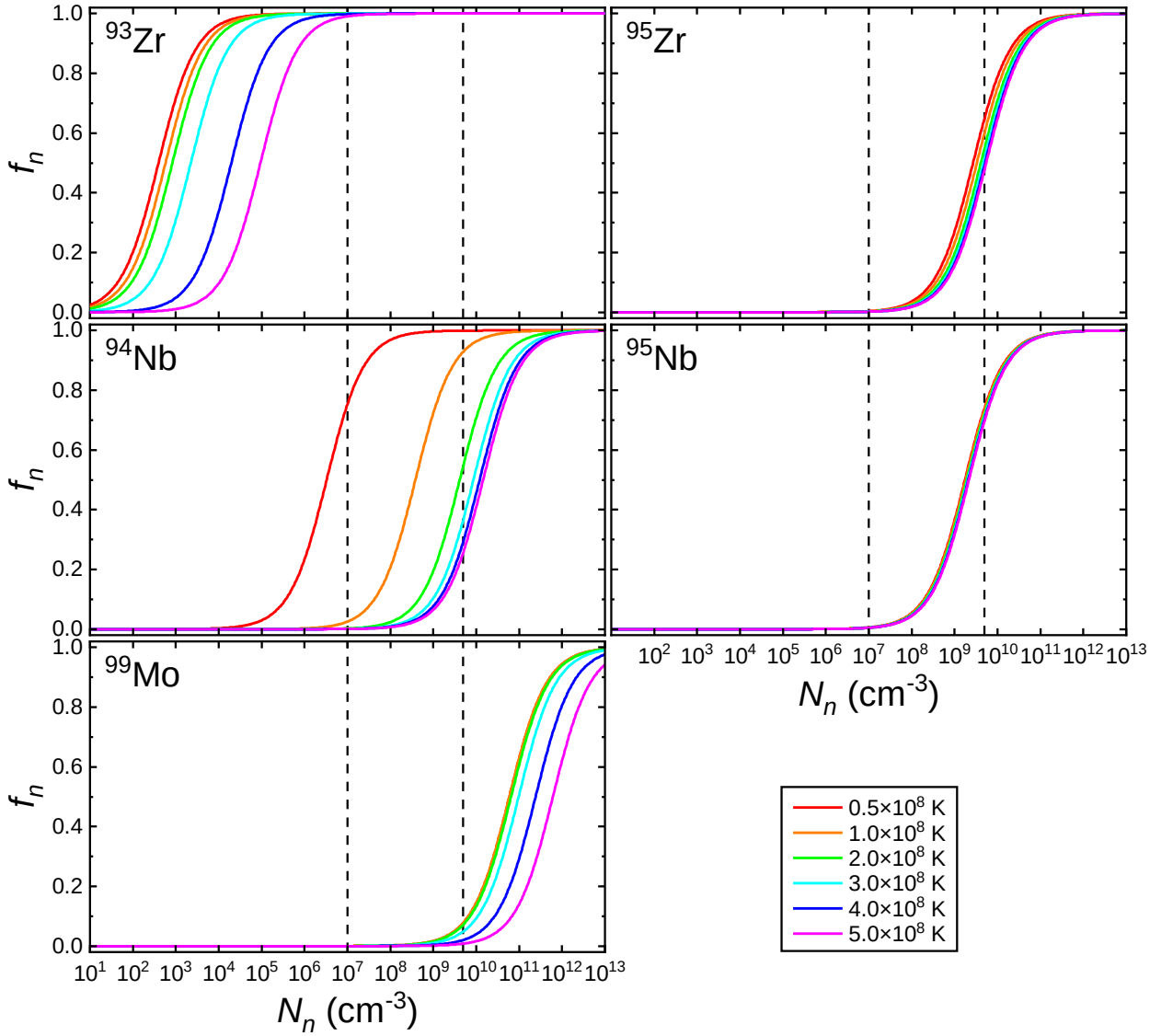

Figure 7. Branching factors $f_n = \lambda_n / (\lambda_n + \lambda_\beta)$ as a function of neutron density N_n and temperature for nuclides relevant in molybdenum nucleosynthesis. We used temperature dependent β-decay rates reported by Takahashi & Yokoi (1987) and interpolated neutron capture cross section for different temperatures using MACS values from KADoNiS v1.0 (Dillmann et al. 2014). For ^{93}Zr, which shows also a slight dependence of the β-decay rates on electron density N_e, we assumed $N_e = 3\times10^{26}$ cm^{-3}. However, the actual value has only a very limited effect on the displayed curves. Vertical dashed lines in the plots at neutron densities of 10^7 cm^{-3} and 5×10^9 cm^{-3} mark the expected maximum neutron densities caused by the ^{13}C(α, n)^{16}O and ^{22}Ne(α, n)^{25}Mg reactions, respectively, in low-mass AGB stars, which should take place at peak temperatures close to 1×10^8 K and 3×10^8 K (see respective color-coded curves in each plot).

While the *s*-process follows the main path shown in Figure 1, several branch points along the way have to be considered in order to understand the observed molybdenum isotope ratios in mainstream SiC grains. Branching factors $f_n = \lambda_n / (\lambda_n + \lambda_\beta)$, where λ_β and λ_n are β-decay and neutron capture rates, respectively, of the relevant nuclides are shown in Figure 7. Some of the β-decay rates and therefore also the branching factors show a strong temperature dependence

(Takahashi & Yokoi 1987). The neutron capture cross sections for the relevant nuclides have only been calculated from theoretical data and should be regarded as rather uncertain, except for ^{93}Zr, for which experimental values exist. The neutron capture cross sections used in these calculations are Maxwellian-averaged cross sections (MACS) from KADoNiS v1.0 (Dillmann et al. 2014), which, for the theoretical data, are quite different from values reported earlier (Dillmann et al. 2006). The temperature dependences of the cross sections according to the values tabulated in KADoNiS v1.0 (Dillmann et al. 2014) were taken into account for generating Figure 7. In the following, we discuss each stable molybdenum isotope relative to ^{96}Mo individually, its relation to the *s*-process, and how the various branch points come into play.

4.2.1. Molybdenum-92

The *p*-process isotope ^{92}Mo can under no circumstances be created in a neutron capture process. On the contrary, the *s*-process effectively consumes any ^{92}Mo initially present, forming ^{93}Mo, which either decays into ^{93}Nb or is transformed, by another neutron capture, to ^{94}Mo. Although the neutron capture cross section for ^{92}Mo is lower than for all other molybdenum isotopes (see Figure 1), it is still highest among stable nuclides with magic neutron number 50, e.g., by more than a factor of 10 higher than for ^{88}Sr. Therefore, ^{92}Mo destruction by the *s*-process in the helium intershell of AGB stars is rather effective.

4.2.2. Molybdenum-94

The *p*-process isotope ^{94}Mo should also be consumed by neutron capture in the helium intershell. However, as discussed by Lugaro et al. (2003), there are three ways to generate some ^{94}Mo during the *s*-process. First, it could be created via two consecutive neutron captures starting from the initial ^{92}Mo, with ^{93}Mo being sufficiently long-lived that another neutron capture could occur before it decays to ^{93}Nb. However, due to its larger neutron capture cross section, ^{94}Mo should be consumed faster than it can be created from ^{92}Mo, which also runs out quickly during the *s*-process. A second way to generate ^{94}Mo would start from the initial ^{93}Nb, which is converted by neutron capture to ^{94}Nb, which then could decay into ^{94}Mo. However, after the initial ^{93}Nb is gone, this path should also run dry. There is a third path, which would also go through ^{93}Nb, which, in this case, would be replenished from the main *s*-process path via the decay of ^{93}Zr. This relatively long-lived nuclide is produced during the *s*-process but usually captures another neutron before it can decay to ^{93}Nb as can be seen from the branching factors in Figure 7. However, ^{93}Zr, freshly produced by the *s*-process, could decay to ^{93}Nb in the interpulse phase, when, for several thousand years for most of the helium intershell, no neutron source exists (see the blue line in Figure 1 of Liu et al. 2018a); remember, the ^{13}C(α, *n*)^{16}O reaction only takes place in the ^{13}C pocket. The ^{93}Nb would then, during the next neutron exposure, be converted to ^{94}Nb, which is another branch point (Figure 1) on the way to ^{94}Mo. It has a relatively long half-life of ~20 ka at room temperature only, but decays much faster at stellar temperatures (~0.5 a half-life at 10^8 K and only ~9 d half-life at 3×10^8 K; Takahashi & Yokoi 1987). The β-decay should therefore dominate over neutron capture under nearly all conditions in the helium intershell (Figure 7).

The amount of ^{94}Mo that is produced by the *s*-process and that is found in our mainstream grains must somewhat depend on the relative timescales of neutron production and neutron-free phases. Let us assume, according to Figure 7, that during any neutron exposure, ^{93}Zr decay can be neglected (Figure 7) and the *s*-process follows its main path (Figure 1). And let us further

assume that the ^{93}Zr that decays to ^{93}Nb when no neutrons are produced is ultimately, during later neutron exposure, transformed via ^{94}Nb into ^{94}Mo, ^{95}Mo, and follows the main *s*-process path from there. In this approach, we are neglecting neutron capture by ^{94}Nb, which is reasonable as discussed above. If we now further assume that isotope ratios approximately depend on the inverse of the cross sections, which is at least expected for nuclides further away from magic neutron numbers, we can make some predictions about the average time a ^{93}Zr atom was given to decay. Since ^{94}Mo and ^{96}Mo have similar cross sections (see Figure 1), their abundances would also be similar if the main ^{96}Mo production would go through ^{94}Mo. Instead, the average *s*-process ratio for these isotopes determined from our mainstream grains is about 1/50 (see Table 2). This would mean that, on average, one out of 50 ^{93}Zr atoms would have had the time to decay. At a half-life of 1.61 Ma (at room temperature), it takes about 47 ka until 1/50 of ^{93}Zr atoms have decayed, and even at a temperature of 10^8 K, it would still take about 35 ka. This appears reasonable when taking into account that the material from the ^{13}C pocket gets diluted between the neutron exposures and the time gaps between neutron exposures in the ^{13}C pocket (Figure 1 of Liu et al. 2018a). However, this assumes that the *s*-process is governed by neutrons from the ^{13}C(α, n)^{16}O reaction in a confined region and not by the ^{22}Ne(α, n)^{25}Mg reaction covering the entire helium intershell and efficiently transforming ^{93}Zr to ^{94}Zr.

From the average ^{94}Mo$_s$ abundance in our mainstream SiC grains (Table 2), it can be concluded that 3.6 % of the solar ^{94}Mo was formed by the *s*-process, which is much higher than the value of 1.0 % suggested by Bisterzo et al. (2014). The significant variation (MSWD = 4.4) observed in the ^{94}Mo$_s$ abundance in our mainstream SiC grains could, however, be explained by variations in the specific timescales of the processes mentioned above or differences in mixing efficiencies during thermal pulses, effectively changing the time for ^{93}Zr decay between neutron exposures. No *s*-process ^{94}Mo at all, which was observed for some grains, could mean that the material the grain condensed from had not seen a second neutron exposure event or had not been given any significant time to let ^{93}Zr decay between consecutive neutron exposures. A single neutron exposure, no matter how long it would last, would not be able to make any significant ^{94}Mo, since there would be no time for ^{93}Zr to decay to ^{93}Nb, which would need a second neutron exposure in order to produce ^{94}Nb and therefore ^{94}Mo.

The variation in *s*-process ^{94}Mo among our grains (Figure 5), and the anticorrelation with *s*-process ^{95}Mo (Figure 6) could be explained by variations in the effective branching at ^{93}Zr caused by relative timescale differences and by some branching at ^{94}Nb, which could occur mainly during the ^{22}Ne(α, n)^{25}Mg reaction (see Figure 7).

4.2.3. Molybdenum-95

From our analysis of mainstream SiC grains (Table 2), it can be concluded that 38.5 % of the solar ^{95}Mo was formed by the *s*-process, which is slightly less than the 45.4 % suggested by Bisterzo et al. (2014). The rest of the solar ^{95}Mo was probably formed by the *r*-process, although some intermediate process responsible for the ^{95}Mo enrichment in SiC grains of type X (Meyer et al. 2000), together with a production of the other mixed *s*- and *r*-process isotopes ^{97}Mo and ^{98}Mo, could also have contributed but would not explain the solar ^{100}Mo abundance.

Together with ^{96}Mo, ^{95}Mo is influenced by the branching at ^{95}Zr, which could play a role during the thermal pulse when the neutron density could reach 5×10^9 cm^{-3} (Figure 7). However, branching at ^{95}Zr cannot explain variation in ^{95}Mo/^{96}Mo since both isotopes would be affected equally. Another branching at ^{95}Nb, which should be activated at similar neutron densities as the

branching at ^{95}Zr (Figure 7) and also lies on the main *s*-process path (Figure 1), could finally lead to some variation in the relative ^{95}Mo/^{96}Mo production. Variation in the neutron production via ^{22}Ne(α, n)^{25}Mg, ultimately depending on temperature and therefore stellar mass, could probably explain some of the relatively large range for $\delta^{95}Mo_{96,s}$ (Figure 5). This range translates to a range of about 0.32–0.41 in ^{95}Mo/^{96}Mo for the *s*-process, which would be hard to explain from branching alone without invoking major variations in ^{97}Mo/^{96}Mo, which have not been observed (Table 2 and Figure 5). However, one should keep in mind that the actual branching strongly depends on the neutron capture cross sections, which are poorly known for these nuclides. If we assume that the ^{95}Nb neutron capture cross section is underestimated while the cross section for ^{95}Zr is overestimated, ^{95}Mo could be bypassed without bypassing ^{96}Mo. This could explain large variations in ^{95}Mo/^{96}Mo, caused by variations in branching at ^{95}Nb, without the need for large ^{97}Mo/^{96}Mo or ^{98}Mo/^{96}Mo variations, which would be caused by branching at ^{95}Zr. Significantly lower neutron capture cross sections for ^{95}Zr have also been suggested in the literature (Toukan & Käppeler 1990; Lugaro et al. 2014; Liu et al. 2014a) and seem to be needed to explain the strong depletions of ^{96}Zr relative to ^{94}Zr observed in mainstream SiC grains (Nicolussi et al. 1997; Barzyk et al. 2007).

However, this model could not explain the observed correlation between *s*-process ^{95}Mo and *s*-process ^{100}Mo relative to ^{96}Mo (Figure 6). Even if we assume that branching at ^{95}Zr is not significant, the relatively high neutron densities required to make significant ^{100}Mo should activate branching at ^{95}Nb and therefore lower ^{95}Mo relative to ^{96}Mo instead of increasing it. If, on the other hand, branching at ^{95}Nb is also not taking place, it would be difficult to explain the variation in ^{95}Mo relative to ^{96}Mo.

Again, fine tuning of some timescales involved could help to explain the observations. If, during a thermal pulse, the ^{22}Ne(α, n)^{25}Mg reaction is sufficiently activated to produce ^{100}Mo but is not activating branching at ^{95}Zr, and, if the peak neutron density of that reaction is only maintained for a relatively short time (comparable to or shorter than the lifetimes of ^{95}Zr and ^{95}Nb) as has been suggested before (see Figure 2 in Lugaro et al. 2003), significant amounts of ^{95}Zr could be produced and would ultimately decay during the interpulse phase to ^{95}Mo, without creating equivalent amounts of ^{96}Mo, ^{97}Mo, and ^{98}Mo.

4.2.4. Molybdenum-96

The *s*-process-only isotope ^{96}Mo is shielded from the *r*-process by ^{96}Zr, which only decays by double beta decay, but not on an astrophysically relevant timescale (Figure 1). Therefore, ^{96}Mo is used here as a reference isotope and not discussed individually.

4.2.5. Molybdenum-97

The *s*-process, as observed in the mainstream SiC grains, could account for 46.8 % of the solar ^{97}Mo, which is another mixed *s*- and *r*-process isotope. This is slightly higher than the 43.3 % suggested by Bisterzo et al. (2014). Variations in the ^{97}Mo/^{96}Mo ratio inferred for the *s*-process for individual grains beyond expected statistical variations have not been observed. On the contrary, an MSWD of 1.0 (Table 2) for the fit through the data points excludes variations beyond a few ‰. If there would be any significant branching at ^{95}Zr, such variation in the relative abundances of ^{96}Mo and ^{97}Mo could not be avoided, because neutron capture of ^{95}Zr would cause bypassing of ^{96}Mo, leading to a relative overabundance of ^{97}Mo and ^{98}Mo, which would not be bypassed (Figure 1). Such an overabundance, however, is not observed in our data.

On the contrary, the relative abundances of ^{96}Mo, ^{97}Mo, and ^{98}Mo calculated for the *s*-process nicely follow the inverse of the cross sections, with a slightly enriched ^{96}Mo abundance, which is no surprise since we are still somewhat close to the magic neutron number $n = 50$. Consequently, either the ^{22}Ne(α, n)^{25}Mg reaction is never fully activated for any of the grains, or the neutron capture cross section for ^{95}Zr has been significantly overestimated.

4.2.6. Molybdenum-98

A similar picture emerges for ^{98}Mo, another mixed *s*- and *r*-process isotope. The *s*-process, as observed in the mainstream SiC grains, could account for 74.4 % of the solar ^{98}Mo, which is higher than the value of 57.5 % suggested by Bisterzo et al. (2014). Variations in the ^{98}Mo/^{96}Mo can again be explained by statistical variations. However, the MSWD of 1.8 for the linear regression is only marginally within the 95 % confidence interval of [0.432, 1.803] for 17 data points in a forced fit. Therefore, we cannot fully exclude that there is some scatter in the data that has not been fully resolved in our measurements and that could not be explained by the linear trend. However, it is premature to speculate on an unresolved effect.

4.2.7. Molybdenum-100

^{100}Mo, usually considered an *r*-process-only isotope, is not produced in major quantities during the *s*-process. However, the branch point at ^{99}Mo allows for some ^{100}Mo production even during the *s*-process. Bisterzo et al. (2014) expected the *s*-process to account for 2.3 % of the solar ^{100}Mo. Our results give a value of 2.0 %, with a range for individual grains of about 0–6 % (Figure 5). This variation (MSWD = 9.3) cannot be explained by statistical variations alone but asks for true variations in the *s*-process leading to ^{100}Mo. The branch point at ^{99}Mo (Figure 1), which shows a strong temperature-dependence (Figure 7), becomes active during the thermal pulse. At a peak temperature of 3×10^8 K and a neutron density of 5×10^9 cm^{-3}, the branching factor f_n is 0.093. Since the relative abundances of ^{96}Mo, ^{97}Mo, and ^{98}Mo calculated for the *s*-process nicely follow the inverse of the cross sections, we would estimate the ^{100}Mo abundance without ^{99}Mo decay to be ~93 times higher than observed. Taking these numbers at face value, we would infer that the ^{22}Ne(α, n)^{25}Mg reaction contributes on average about a factor of eight less neutrons to the *s*-process in AGB stars than the ^{13}C(α, n)^{16}O reaction. This number has a large uncertainty because it strongly depends on the branching factor and therefore on the temperature, neutron density, and the exact neutron capture cross section, which has only been derived from theoretical calculations. The wide range of $\delta^{100}Mo_{96,s}$ for our mainstream SiC grains clearly shows that the ^{22}Ne(α, n)^{25}Mg reaction gets activated to different degrees in the various parent stars of these grains.

4.3. AB Grain

Among the analyzed presolar SiC grains was one grain classified as type AB2. A ^{12}C/^{13}C ratio below 10 identifies it as an AB grain, and a ^{14}N/^{15}N ratio 2.5 times above the solar ratio of ~440 identifies it as an AB2 grain, if we follow the classification scheme suggested by Liu et al. (2017a, b). It has, however, been suggested that AB2 grains should lack *s*-process enhancements for elements like strontium, molybdenum, and barium (Liu et al. 2017b). This disagrees with the results for our grain, which clearly shows an *s*-process pattern not only for molybdenum but also for strontium and barium (Table 1). Furthermore, except for ^{94}Mo, all molybdenum isotopes of the AB grain are in perfect agreement with the trend for the mainstream grains. Therefore, J-type

carbon stars, which have been suggested by Liu et al. (2017b) as a dominant source for AB2 grains, can be excluded as origin for our grain, since grains from those stars should not show any *s*-process enhancement. Furthermore, Liu et al. (2017b) excluded born-again AGB stars (Asplund et al. 1999), which had previously been suggested as one source for AB grains. The apparent depletion in ^{94}Mo in our AB2 grain compared to mainstream grains, with all other molybdenum isotopes in accordance, however, could mean that the *s*-process in this grain's parent star did not occur in many consecutive pulses but was governed by one large neutron burst as predicted for born-again AGB stars. However, the neutron density expected for such a process would be of the order of 10^{15} cm^{-3} (Herwig et al. 2011), which should also lead to a significant ^{100}Mo enrichment, which has not been observed for our grain.

Strictly speaking, the extrapolated $\delta^{94}Mo_{96,s}$ value for our AB2 grain would be at a nonsensical value below –1000 ‰ (Figure 5). However, if the grain has some very small residual *p*-process ^{92}Mo from its parent star, an extrapolation to δ^{92}Mo = –1000 ‰ to calculate $\delta^{94}Mo_{96,s}$ would not be justified. Interestingly, there is one detection of a *p*-process enrichment found in one AB grain (Savina et al. 2003c) that was also identified later as an AB2 grain (Liu et al. 2017b). However, considering that there is only the one measurement of an AB2 grain presented here that has such a small analytical error, it seems premature to draw too many conclusions about the origin of AB2 grains in general. However, to fully explain AB grains, perhaps more than two different stellar sources are needed, e.g., born-again AGB stars, J-type carbon stars, and Type II supernovae, and a subdivision based on nitrogen isotopes alone is not sufficient.

5. Conclusions

We obtained molybdenum isotope data, together with data on strontium and barium isotopes, from 17 mainstream silicon carbide grains and from one AB grain using CHILI, and complementary NanoSIMS isotope data for grain classification. The molybdenum isotope data have an unprecedented precision that provides the best estimate for *s*-process molybdenum made in low-mass AGB stars so far. Furthermore, a small but significant variability was observed between individual grains for *s*-process ^{94}Mo, ^{95}Mo, and ^{100}Mo relative to the other stable molybdenum isotopes, ^{96}Mo, ^{97}Mo, and ^{98}Mo, which showed no significant variability in their *s*-process signature. Furthermore, variation in *s*-process ^{95}Mo seems to be positively correlated with variations in ^{100}Mo and negatively correlated with variations in ^{94}Mo, respectively, both of which are made in small quantities also by the *s*-process. This could all be explained by subtle differences in branching between neutron capture and β-decay at ^{93}Zr, ^{94}Nb, ^{95}Nb, and ^{99}Mo, which depends strongly on neutron densities, temperatures, timescales, and material mixing in the helium intershell during the AGB phase of the grains' parent stars where the *s*-process took place in thermal pulses. Branching at ^{95}Zr, however, seems not to be significantly activated during these processes, which could be explained if its neutron capture cross section has been vastly overestimated, so that neutron capture played no significant role.

The AB grain, which would classify as an AB2 grain, following the scheme proposed by Liu et al. (2017b), shows an almost identical *s*-process signature as the mainstream grains, with the exception in *s*-process ^{94}Mo, which does not appear to be present. This seems to contradict J-type carbon stars as a possible source at least for our AB2 grain. Future explanations for the origin of

AB grains should take this data into account. However, more high-precision molybdenum data would be desirable for a better understanding of these grains.

This also holds in general for other presolar grain types. The increased precision of CHILI presents new opportunities for studying stardust, which could provide new major insights into stellar nucleosynthesis.

Finally, the observation that molybdenum isotopes in presolar SiC mainstream, AB1, AB2, Y, and Z grains all consistently seem to follow the same mixing lines between a pure *s*-process endmember and solar compositions, suggests that *r*- and *p*-processes occur at a fixed rate throughout time and space, probably triggered by the very same stellar events.

We are deeply grateful to Patrick Boehnke for his contributions to the CHILI measurements and for helpful discussions. The manuscript benefitted significantly from very detailed and constructive comments by an anonymous reviewer. We also acknowledge Roberto Gallino for his adept remarks. We thank Elmar Gröner for technical support on the NanoSIMS. This work was supported by NASA (grants NNX15AF78G, 80NSSC17K0250, and 80NSSC17K0251 to AMD). LLNL-JRNL-768104.

ORCID iDs

Thomas Stephan https://orcid.org/0000-0001-6377-8731
Reto Trappitsch https://orcid.org/0000-0002-0924-236X
Peter Hoppe https://orcid.org/0000-0003-3681-050X
Andrew M. Davis https://orcid.org/0000-0001-7955-6236
Michael J. Pellin https://orcid.org/0000-0002-8149-9768

References

Alexander, C. M. O'D. 1993, GeCoA, 57, 2869
Amari, S., Lewis, R. S., & Anders, E. 1994, GeCoA, 58, 459
Amari, S., Nittler, L. R., Zinner, E., Lodders, K., & Lewis, R. S. 2001, ApJ, 559, 463
Asplund, M., Lambert, D. L., Kipper, T., Pollacco, D., & Shetrone, M. D. 1999, A&A, 343, 507
Audi, G., Kondev, F. G., Wang, M., et al. 2012, ChPhC, 36, 1157
Ávila, J. N., Ireland, T. R., Gyngard, F., et al. 2013, GeCoA, 120, 628
Barzyk, J. G., Savina, M. R., Davis, A. M., et al. 2007, M&PS, 42, 1103
Battistini, C., & Bensby, T. 2016, A&A, 586, A49
Bernatowicz, T. J., Cowsik, R., Gibbons, P. C., et al. 1996, ApJ, 472, 760
Bisterzo, S., Gallino, R., Straniero, O., Cristallo, S., & Käppeler, F. 2011, MNRAS, 418, 284
Bisterzo, S., Travaglio, C., Gallino, R., Wiescher, M., & Käppeler, F. 2014, ApJ, 787, 10
Bisterzo, S., Travaglio, C., Wiescher, M., Käppeler, F., & Gallino, R. 2017, ApJ, 835, 97

Bliss, J., Arcones, A., & Qian, Y.-Z. 2018, ApJ, 866, 105
Budde, G., Burkhardt, C., Brennecka, G. A., et al. 2016, E&PSL, 454, 293
Budde, G., Kruijer, T. S., & Kleine, T. 2018, GeCoA, 222, 284
Burkhardt, C., Kleine, T., Dauphas, N., & Wieler, R. 2012, E&PSL, 357–358, 298
Burkhardt, C., Kleine, T., Oberli, F., et al. 2011, E&PSL, 312, 390
Busso, M., Gallino, R., & Wasserburg, G. J. 1999, ARA&A, 37, 239
Clayton, D. D. 1997, ApJL, 484, L67
Clayton, D. D. 2003, LPI, 34, #1059
Clayton, D. D., & Timmes, F. X. 1997, ApJ, 483, 220
Cristallo, S., Straniero, O., Gallino, R., et al. 2009, ApJ, 696, 797
Dauphas, N., Marty, B., & Reisberg, L. 2002, ApJL, 569, L139
Davis, A. M. 2011, PNAS, 108, 19142
Dillmann, I., Heil, M., Käppeler, F., et al. 2006, AIPC, 819, 123
Dillmann, I., Szücs, T., Plag, R., et al. 2014, NDS, 120, 171
Fairbank, W. M., Jr., Spaar, M. T., Parks, J. E., & Hutchinson, J. M. R. 1989, PhRvA, 40, 2195
Farouqi, K., Kratz, K.-L., & Pfeiffer, B. 2009, PASA, 26, 194
Gallino, R., Raiteri, C. M., Busso, M., & Matteucci, F. 1994, ApJ, 430, 858
Gyngard, F., Amari, S., Zinner, E., & Ott, U. 2009, ApJ, 694, 359
Heck, P. R., Greer, J., Kööp, L., et al. 2019, PNAS, submitted
Heck, P. R., Gyngard, F., Ott, U., et al. 2009, ApJ, 698, 1155
Herwig, F., Pignatari, M., Woodward, P. R., et al. 2011, ApJ, 727, 89
Hoffman, R. D., Woosley, S. E., Fuller, G. M., & Meyer, B. S. 1996, ApJ, 460, 478
Hoppe, P., Amari, S., Zinner, E., Ireland, T., & Lewis, R. S. 1994, ApJ, 430, 870
Hoppe, P., Cohen, S., & Meibom, A. 2013, Geostandards and Geoanalytical Research, 37, 111
Hoppe, P., Fujiya, W., & Zinner, E. 2012, ApJL, 745, L26
Hoppe, P., Leitner, J., Gröner, E., et al. 2010, ApJ, 719, 1370
Hoppe, P., Leitner, J., & Kodolányi, J. 2018, ApJ, 869, 47
Hoppe, P., Lodders, K., & Fujiya, W. 2015, M&PS, 50, 1122
Hoppe, P., Strebel, R., Eberhardt, P., Amari, S., & Lewis, R. S. 1996, GeCoA, 60, 883
Huss, G. R., Hutcheon, I. D., & Wasserburg, G. J. 1997, GeCoA, 61, 5117
Kruijer, T. S., Burkhardt, C., Budde, G., & Kleine, T. 2017, PNAS, 114, 6712
Levine, J., Savina, M. R., Stephan, T., et al. 2009, IJMSp, 288, 36
Lewis, R. S., Srinivasan, B., & Anders, E. 1975, Sci, 190, 1251
Lewis, R. S., Tang, M., Wacker, J. F., Anders, E., & Steel, E. 1987, Natur, 326, 160
Liu, N., Gallino, R., Bisterzo, S., et al. 2014a, ApJ, 788, 163
Liu, N., Gallino, R., Cristallo, S., et al. 2018a, ApJ, 865, 112
Liu, N., Nittler, L. R., Alexander, C. M. O'D., et al. 2016, ApJ, 820, 140
Liu, N., Nittler, L. R., Pignatari, M., Alexander, C. M. O'D., & Wang, J. 2017a, ApJL, 842, L1

Liu, N., Savina, M. R., Davis, A. M., et al. 2014b, ApJ, 786, 66
Liu, N., Savina, M. R., Gallino, R., et al. 2015, ApJ, 803, 12
Liu, N., Stephan, T., Boehnke, P., et al. 2017b, ApJL, 844, L12
Liu, N., Stephan, T., Boehnke, P., et al. 2018b, ApJ, 855, 144
Liu, N., Stephan, T., Cristallo, S., et al. 2019, ApJ, submitted
Lugaro, M., Davis, A. M., Gallino, R., et al. 2003, ApJ, 593, 486
Lugaro, M., Tagliente, G., Karakas, A. I., et al. 2014, ApJ, 780, 95
Mahon, K. I. 1996, IGRv, 38, 293
Marhas, K. K., Amari, S., Gyngard, F., Zinner, E., & Gallino, R. 2008, ApJ, 689, 622
Marhas, K. K., Hoppe, P., & Ott, U. 2007, M&PS, 42, 1077
Marty, B., Chaussidon, M., Wiens, R. C., Jurewicz, A. J. G., & Burnett, D. S. 2011, Sci, 332, 1533
Meija, J., Coplen, T. B., Berglund, M., et al. 2016, PApCh, 88, 293
Meshik, A. P., Pravdivtseva, O. V., & Hohenberg, C. M. 2001, LPI, 32, #2158
Meyer, B. S., Clayton, D. D., & The, L.-S. 2000, ApJL, 540, L49
Nicolussi, G. K., Davis, A. M., Pellin, M. J., et al. 1997, Sci, 277, 1281
Nicolussi, G. K., Pellin, M. J., Lewis, R. S., et al. 1998a, GeCoA, 62, 1093
Nicolussi, G. K., Pellin, M. J., Lewis, R. S., et al. 1998b, PhRvL, 81, 3583
Nittler, L. R., & Alexander, C. M. O'D. 2003, GeCoA, 67, 4961
Nittler, L. R., & Ciesla, F. 2016, ARA&A, 54, 53
Nittler, L. R., & Hoppe, P. 2005, ApJL, 631, L89
Ott, U., & Begemann, F. 1990a, ApJL, 353, L57
Ott, U., & Begemann, F. 1990b, LPI, 21, 920
Pellin, M. J., Savina, M. R., Calaway, W. F., et al. 2006, LPI, 37, #2041
Podosek, F. A., Prombo, C. A., Amari, S., & Lewis, R. S. 2004, ApJ, 605, 960
Prombo, C. A., Podosek, F. A., Amari, S., & Lewis, R. S. 1993, ApJ, 410, 393
Reynolds, J. H., & Turner, G. 1964, JGR, 69, 3263
Savina, M. R., Davis, A. M., Tripa, C. E., et al. 2003a, GeCoA, 67, 3201
Savina, M. R., Pellin, M. J., Tripa, C. E., et al. 2003b, GeCoA, 67, 3215
Savina, M. R., Tripa, C. E., Pellin, M. J., et al. 2003c, LPI, 34, #2079
Stephan, T., Trappitsch, R., Davis, A. M., et al. 2016, IJMSp, 407, 1
Stephan, T., Trappitsch, R., Davis, A. M., et al. 2018, GeCoA, 221, 109
Stephan, T., Zehnpfenning, J., & Benninghoven, A. 1994, JVSTA, 12, 405
Straniero, O., Gallino, R., & Cristallo, S. 2006, NuPhA, 777, 311
Takahashi, K., & Yokoi, K. 1987, ADNDT, 36, 375
Toukan, K. A., & Käppeler, F. 1990, ApJ, 348, 357
Xu, Y., Zinner, E., Gallino, R., et al. 2015, ApJ, 799, 156
Yin, Q.-Z., Lee, C.-T. L., & Ott, U. 2006, ApJ, 647, 667

York, D. 1969, E&PSL, 5, 320

Zinner, E. K. 2014, in Meteorites and Cosmochemical Processes, ed. A. M. Davis, Treatise on Geochemistry 2nd Ed, exec. eds. H. D. Holland & K. K.Turekian (Oxford: Elsevier), 181

Zinner, E., Amari, S., & Lewis, R. S. 1991, ApJL, 382, L47